ADVANCED ENERGY MATERIALS
www.advenergymat.de

Hybrid Transverse Magneto-Thermoelectric Cooling in Artificially Tilted Multilayers

Ken-ichi Uchida, Takamasa Hirai, Fuyuki Ando, and Hossein Sepehri-Amin*

In artificially tilted multilayers comprising two different conductors that are alternately and obliquely stacked, transverse thermoelectric conversion occurs, in which charge and heat currents are interconverted in the orthogonal direction. Although transverse thermoelectric conversion also occurs in homogeneous materials as an intrinsic transport phenomenon owing to the effects of magnetic fields, magnetization, and spins on conduction carriers, such magneto-thermoelectric effects are investigated independently of thermoelectrics for artificially tilted multilayers. Here, this study shows that the synergy of these different principles improves the performance of transverse thermoelectric conversion. Using lock-in thermography techniques, transverse thermoelectric conversion processes are visualized in artificially tilted multilayers and the experiments clarify how nonuniform charge currents are converted into orthogonal heat currents. Through the measurements of temperature change under magnetic fields, the contributions of the magneto-thermoelectric effects are quantified in the artificially tilted multilayers and magnetically enhanced hybrid transverse thermoelectric cooling is demonstrated. By replacing one of the conductors in the multilayer with permanent magnets, the same functionality is obtained even in the absence of magnetic fields, paving the way for the creation of "thermoelectric permanent magnets" that exhibit efficient transverse thermoelectric conversion together with spontaneous magnetization. This study provides a new material design guideline for transverse thermoelectrics.

1. Introduction

Thermoelectric cooling is a promising technology for the efficient thermal management of electronic devices.[1] Conventional thermoelectric cooling is driven by the Peltier effect, in which a charge current $\mathbf{J}_\mathrm{c}$ applied to a conductor is converted into a heat current $\mathbf{J}_\mathrm{q}$. Because of the parallel relationship between $\mathbf{J}_\mathrm{c}$ and $\mathbf{J}_\mathrm{q}$, the Peltier effect is classified as a longitudinal thermoelectric effect. Due to the longitudinal geometry, a thermoelectric module based on the Peltier effect usually consists of many pairs of *p*- and *n*-type conductors arranged alternately and connected in series. Such a complex 3D structure consisting of many junctions often has problems such as low mechanical durability, high manufacturing costs, and efficiency losses due to contact resistances.[2] These issues limit the applicability of thermoelectric cooling technologies. The same problems apply to thermoelectric power generation based on the Seebeck effect.

Research on transverse thermoelectric effects is gaining momentum with the aim of improving the versatility of thermoelectric conversion technologies and expanding their applications.[3] Transverse thermoelectric effects allow the interconversion between $\mathbf{J}_\mathrm{c}$ and $\mathbf{J}_\mathrm{q}$ in the orthogonal direction. Owing to this feature, simple and versatile thermoelectric cooling as well as power generation can be achieved. The output power of transverse thermoelectric conversion can be increased by increasing the size of materials without constructing complex 3D structures, and the energy losses due to intermediated electrodes and substrates can be reduced. Although transverse thermoelectric conversion has many advantages, it is still in the basic research phase owing to various issues; e.g., its thermopower has not reached a practical level.

Transverse thermoelectric conversion is driven by six principles that can be broadly classified into phenomena occurring in homogeneous materials and those occurring in hybrid/composite materials.[3] The former phenomena include the ordinary and anomalous Nernst/Ettingshausen effects[4–12] and goniopolarity,[13] while the latter includes the spin Seebeck/Peltier effect[14–16] and Seebeck/Peltier-driven transverse thermoelectric conversion in magnetic/thermoelectric hybrid materials[17] and in artificially tilted multilayers.[18–27] As typified by the Nernst/Ettingshausen effects, most transverse thermoelectric effects appear in conductors under external magnetic fields or in magnetic materials with spontaneous magnetization, and these effects have been actively investigated in

K. Uchida, T. Hirai, F. Ando, H. Sepehri-Amin
National Institute for Materials Science
Tsukuba 305-0047, Japan
E-mail: uchida.kenichi@nims.go.jp

The ORCID identification number(s) for the author(s) of this article can be found under https://doi.org/10.1002/aenm.202302375

DOI: 10.1002/aenm.202302375

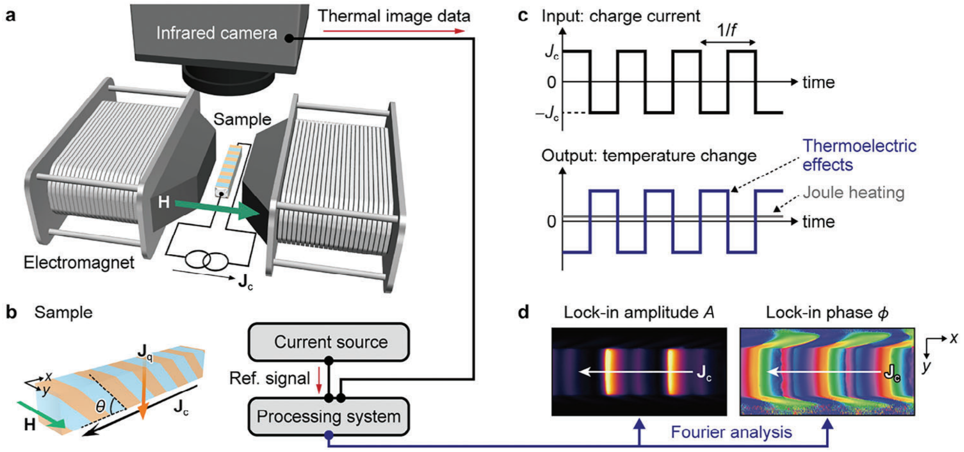

Figure 1. LIT measurements of thermoelectric effects in an artificially tilted multilayer. a) Schematic of the measurement setup for LIT. $\mathbf{J}_c$ denotes a charge current applied to a sample. By using an electromagnet, a magnetic field $\mathbf{H}$ with magnitude H was applied to a sample in the transverse direction, i.e., y direction. b) Schematic of the artificially tilted multilayer sample. The blue and orange parts of the sample correspond to $Bi_{88}Sb_{12}$ and $Bi_{0.2}Sb_{1.8}Te_3$, respectively, for the samples used for Figures 2–7. $\mathbf{J}_q$ and θ denote the net direction of a heat current generated by the transverse thermoelectric effects and tilt angle in the artificially tilted multilayer. c) Input charge current and output temperature changes induced by the thermoelectric effects and Joule heating during the LIT measurements. f and J_c represent the frequency and amplitude of the square-wave-modulated alternating charge current applied to the sample, respectively. In all the LIT measurements, we fixed $J_c = 1$ A. d) Example of the lock-in amplitude A and phase ϕ images for the artificially tilted $Bi_{88}Sb_{12}/Bi_{0.2}Sb_{1.8}Te_3$ multilayer.

the fields of spin caloritronics[28–30] and topological materials science.[9,12] In contrast, transverse thermoelectric conversion in goniopolar materials and artificially tilted multilayers does not require magnetic fields or magnetization and appear due to anisotropic carrier conduction originating from anisotropic crystalline and artificial structures, respectively, i.e., the off-diagonal Seebeck/Peltier effect. Despite having similar functionalities, these transverse thermoelectric conversion phenomena have been studied independently. Their interdisciplinary fusion will bring innovation to transverse thermoelectrics, potentially solving the technological problems associated with thermoelectric converters.

In this study, we demonstrate hybrid transverse thermoelectric cooling by superimposing magneto-thermoelectric effects on artificially tilted multilayers. Using thermoelectric imaging techniques based on lock-in thermography (LIT),[16,31,32] we experimentally visualize the transverse thermoelectric cooling processes due to the structure-induced off-diagonal Peltier effect (ODPE) in artificially tilted multilayers. When the multilayers exhibit the magneto-Peltier effect (MPE)[33] and ordinary Ettingshausen effect (OEE),[4–7] LIT-based thermoelectric imaging under magnetic fields allows us to separate the temperature change signals due to structure-induced ODPE from those due to MPE and OEE and to estimate each contribution quantitatively. An appropriate design of the multilayer structure and magnetic-field direction $\mathbf{H}$ considering the symmetry of the magneto-thermoelectric effects makes it possible to improve the performance of transverse thermoelectric cooling through the hybridization of multiple phenomena. This result provides a novel guideline for increasing the thermopower and figure of merit of transverse thermoelectric conversion, leading to the development of versatile and efficient thermal management technologies.

2. Results and Discussion

2.1. Thermoelectric Conversion Mechanism and Sample System

The artificially tilted multilayer for transverse thermoelectric conversion consists of two different conductors that are stacked obliquely and alternately (**Figure 1**b). In this structure, anisotropic conduction of electrons and holes results in the finite off-diagonal terms of the thermoelectric transport tensor, making the multilayer into a transverse thermoelectric converter.[18–27] In other words, transverse thermoelectric conversion in the artificially tilted multilayer originates from the anisotropic structure itself, and is driven by the longitudinal Seebeck/Peltier effect. This process occurs to the maximum degree when one of the constituent materials is a p-type thermoelectric material and the other is an n-type material but occurs even with the same carrier type when the magnitude of the Seebeck/Peltier coefficient is different from each other. Transverse thermoelectric generation using such multilayers has been studied for many years, and the transverse thermopower and figure of merit can be designed by selecting appropriate constituent materials and optimizing the tilt angle and device geometry.[18–27] Transverse thermoelectric conversion has been demonstrated in not only macroscale bulk materials but also nanoscale superlattices with tilted structures, which are often referred to as $(p \times n)$-type multilayers,[34,35] although we focus only on bulk stacks in this study. However, the contributions of the magneto-thermoelectric effects in artificially tilted multilayers have not been investigated.

How do the magneto-thermoelectric effects contribute to transverse thermoelectric conversion in artificially tilted multilayers? In the following, we focus our discussion on charge-current-induced temperature modulation processes, with an emphasis on their deployment in thermoelectric cooling. First,

Table 1. Transport coefficients of $Bi_{88}Sb_{12}$, $Bi_{0.2}Sb_{1.8}Te_3$, and $Nd_2Fe_{14}B$-type magnet used in this study. σ, κ, $S_{S(N)}$, and $Z_{S(N)}T$ represent the electrical conductivity, thermal conductivity, Seebeck (Nernst) coefficient, and dimensionless figure of merit for the Seebeck (Nernst) effect with T being the absolute temperature, respectively.

Material	$Bi_{88}Sb_{12}$		$Bi_{0.2}Sb_{1.8}Te_3$		$Nd_2Fe_{14}B$-type magnet	
Magnetic field/state	0 T	0.8 T	0 T	0.8 T	Demagnetized	Magnetized
σ (10^5 S m^{-1})	5.88	4.90	1.38	1.38	7.82	7.78
κ (W m^{-1} K^{-1})	4.7	4.3	1.0	1.0	6.9	7.1
S_S (10^{-6} V K^{-1})	−86.7	−108.6	171.0	170.4	−5.9	−6.0
S_N (10^{-6} V K^{-1})	n.a.	−15.6	n.a.	−1.7	n.a.	−0.9
Z_ST at 300 K	0.28	0.40	1.23	1.22	1.2×10^{-3}	1.2×10^{-3}
Z_NT at 300 K	n.a.	8.3×10^{-3}	n.a.	1.2×10^{-4}	n.a.	2.5×10^{-5}

recall that MPE refers to the magnetic-field dependence of the Peltier effect and that OEE refers to the generation of $\mathbf{J}_q$ in the direction of the cross product of $\mathbf{J}_c$ and $\mathbf{H}$, both of which appear in conductors under magnetic fields. The transverse thermoelectric conversion performance due to structure-induced ODPE can increase directly when the Peltier coefficient increases owing to MPE, where it also depends on the electrical and thermal magnetoresistances. Furthermore, if the constituent materials of the multilayers exhibit OEE, the Ettingshausen heat current can be superimposed on structure-induced ODPE by properly selecting the direction of $\mathbf{H}$ to follow the symmetry of OEE. The combination of these processes is the simplest hybrid transverse magneto-thermoelectric conversion. Although this study focuses on the magnetic-field-induced effects, similar hybrid transverse thermoelectric conversion via anisotropic MPE[32] and the anomalous Ettingshausen effect[10,32] can be expected if $\mathbf{H}$ is replaced with magnetization using magnetic materials.

In this study, we demonstrate hybrid transverse magneto-thermoelectric cooling based on a combination of structure-induced ODPE, MPE, and OEE. The main samples used are artificially tilted $Bi_{88}Sb_{12}/Bi_{0.2}Sb_{1.8}Te_3$ multilayers, where $Bi_{88}Sb_{12}$ is an *n*-type thermoelectric material with large MPE and OEE and $Bi_{0.2}Sb_{1.8}Te_3$ is a *p*-type thermoelectric material with a large figure of merit for the Peltier effect. We confirmed that our $Bi_{88}Sb_{12}$ slabs exhibit a large magnetoresistance, MPE, and OEE comparable to previous results[36,37] and our $Bi_{0.2}Sb_{1.8}Te_3$ slabs exhibit no magnetoresistance and MPE and small OEE (Figures S1, S2, Supporting Information). We prepared two artificially tilted $Bi_{88}Sb_{12}/Bi_{0.2}Sb_{1.8}Te_3$ multilayers with a tilt angle of $\theta = 45°$ and a layer thickness of $t = 1.0$ mm (Sample A) and with $\theta = 21°$ and $t = 0.5$ mm (Sample B) by a spark plasma sintering (SPS) method, as described in Section 4. Sample A was designed to optimize the magnetic-field-independent ODPE contribution (Figure S3, Supporting Information). To check the dependence of the magneto-thermoelectric effects in the artificially tilted multilayers on θ, Sample B was also prepared, which has a smaller transverse thermopower, larger effective electrical conductivity along the charge current, and smaller effective thermal conductivity along the heat current. In Section 2.6, to demonstrate the zero-field operation of the hybrid transverse magneto-thermoelectric conversion, we also use an artificially tilted multilayer based on permanent magnets, in which the $Bi_{0.2}Sb_{1.8}Te_3$ layers are replaced with $Nd_2Fe_{14}B$-type magnets, with $\theta = 26°$ and $t = 0.5$ mm (Sample C). The transport properties of our $Bi_{88}Sb_{12}$, $Bi_{0.2}Sb_{1.8}Te_3$, and $Nd_2Fe_{14}B$-type magnet are presented in **Table 1**.

2.2. Visualization of Off-Diagonal Peltier Effect in Artificially Tilted Multilayers

Transverse thermoelectric conversion processes in artificially tilted multilayers have been investigated using finite-element calculations[22,25] but have not been directly observed experimentally. Here, we clarify how nonuniform charge currents in artificially tilted multilayers generate transverse heat currents using the LIT technique, which makes it possible to visualize the spatial distribution and temporal response of temperature modulation induced by thermoelectric effects with high temperature and spatial resolutions.[16,31,32] In the LIT measurements, when a periodic charge current is applied to a sample, thermal images oscillating at the same frequency as the current are extracted through Fourier analysis (Figure 1a). The thermal images obtained are transformed into lock-in amplitude A and phase ϕ images (Figure 1d). The A image shows the distribution of the magnitude of the current-induced temperature modulation and the ϕ image shows the distribution of the sign of the temperature modulation as well as the time delay due to thermal diffusion. To observe the thermoelectric effects using the LIT method, we measured the spatial distribution of infrared radiation thermally emitted from the surface of the sample using an infrared camera while applying a rectangularly-modulated alternating charge current with amplitude J_c (= 1 A), frequency f, and zero offset to the sample along the x direction. By extracting the first-harmonic response of the detected thermal images, we can separate the contribution of the thermoelectric effects ($\propto J_c$) from that of Joule heating ($\propto J_c^2$) because Joule heating generated by such an alternating current is constant over time (Figure 1c). By increasing f, we can identify heat-source positions owing to the reduction in the heat diffusion length, and clarify how the Peltier heat generated locally at the junction interfaces gives rise to transverse thermoelectric conversion. The detected infrared radiation is converted into temperature information through the calibration described in ref. [32]. During the LIT measurements, an in-plane $\mathbf{H}$ (with magnitude H) was applied along the y direction (Figure 1a,b). All the LIT measurements were performed at room temperature and atmospheric pressure.

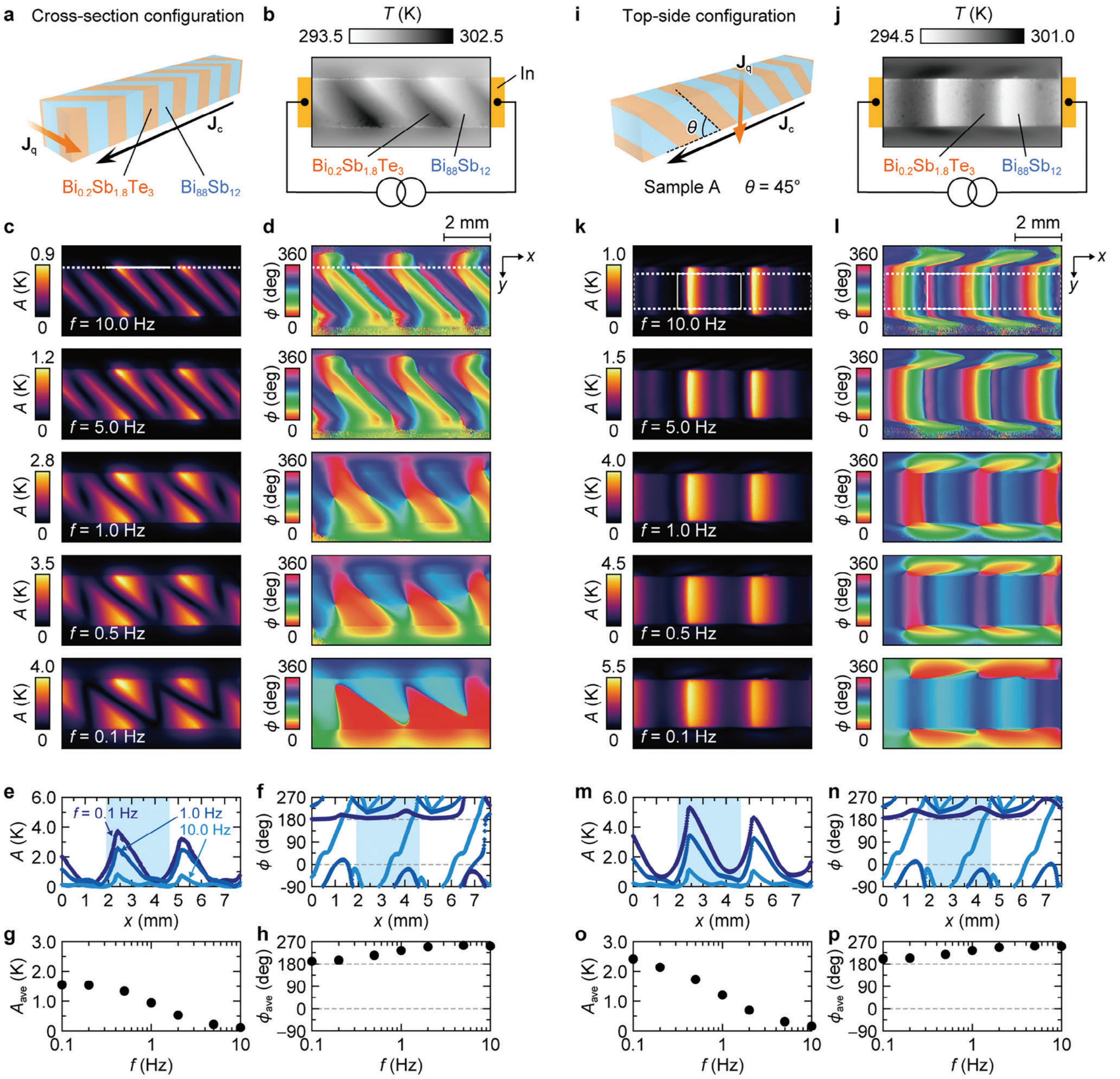

Figure 2. Transverse thermoelectric conversion at zero magnetic field. a) Schematic of Sample A, i.e., the artificially tilted $Bi_{88}Sb_{12}/Bi_{0.2}Sb_{1.8}Te_3$ multilayer with $\theta = 45°$ and 1.0-mm-thick layers, in the cross-section configuration. b) Steady-state temperature T image for Sample A during the LIT measurement in the cross-section configuration. c,d) A (c) and ϕ (d) images for Sample A for different values of f in the cross-section configuration. e,f) x-directional A and ϕ profiles along the white dotted lines in the images in (c,d), respectively. g,h) f dependence of the amplitude A_{ave} and phase ϕ_{ave} averaged over one $Bi_{88}Sb_{12}/Bi_{0.2}Sb_{1.8}Te_3$ pair. i–p) Results for the top-side configuration. The data points in (g,h) [(o,p)] were obtained by averaging the temperature modulation signals in the areas defined by the white rectangles with a size of 183 × 4 (183 × 101) pixels in (c,d) [(k,l)], respectively.

Figure 2 shows the results of the LIT measurements for Sample A in the absence of a magnetic field. First, we measured the current-induced temperature modulation in a cross-sectional configuration (Figure 2a,b). The LIT images at high lock-in frequencies, for example, $f = 10.0$ Hz, indicate that the heating/cooling signals are localized near the junction interfaces between $Bi_{88}Sb_{12}$ and $Bi_{0.2}Sb_{1.8}Te_3$. Here, the A signals exhibit maxima along the oblique interfaces (Figure 2c), whereas the ϕ values at the positions of the A peaks vary by 180° for the neighboring interfaces (Figure 2d). This is indeed the behavior exhibited by temperature modulation due to the Peltier effect. Importantly, as shown in the top image in Figure 2c, the magnitude of the A signals is nonuniform along the oblique junction interfaces, indicating that the charge current flows nonuniformly in the artificially tilted multilayers: this is the origin of the transverse thermoelectric conversion. These local heat release/absorption

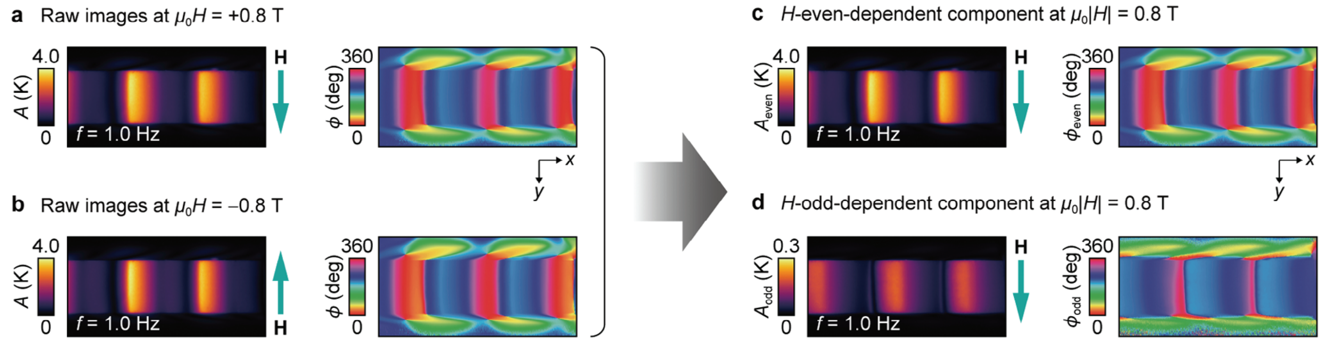

Figure 3. Separation of magneto-thermoelectric effects showing even and odd dependences on magnetic fields. a,b) A and ϕ images for Sample A at $f = 1.0$ Hz in the top-side configuration, measured when the magnetic field with $\mu_0H = 0.8$ T (a) and −0.8 T (b) was applied along the y direction. μ_0 denotes the vacuum permeability. c) A_{even} and ϕ_{even} images calculated from the raw images in (a,b). d) A_{odd} and ϕ_{odd} images calculated from the raw images in (a,b). A_{even} (A_{odd}) and ϕ_{even} (ϕ_{odd}) denote the lock-in amplitude and phase showing the H-even (H-odd) dependence, respectively.

sources are broadened by thermal diffusion as f decreases. The A image at $f = 0.1$ Hz, which reflects a nearly steady-state temperature distribution, shows triangle-patterned signals with an angle corresponding to $\theta = 45°$, and the ϕ values vary from ≈0° (red regions) to ≈180° (blue regions) along the y direction (see the bottom images in Figure 2c,d). As indicated by the line profiles in Figure 2f, the ϕ values along the white dotted line in Figure 2d are almost uniformly 180° at $f = 0.1$ Hz, indicating that the entire surface is cooled by the longitudinal charge current in the steady state. This behavior is evident in the results for the top-side configuration (Figure 2i–n); the almost uniform ϕ values in the bottom image in Figure 2l confirm that the alternately tilted multilayer functions as the transverse thermoelectric converter, although the A values change periodically along the x direction owing to the junction structures.

Figure 2g,h (2o,p) shows the f dependence of the A and ϕ values averaged over one $Bi_{88}Sb_{12}/Bi_{0.2}Sb_{1.8}Te_3$ pair, which are denoted as A_{ave} and ϕ_{ave}, respectively, in the cross-section (top-side) configuration, where the averaged area is marked with a white rectangle in Figure 2c (2k) (note that the rectangle in Figure 2c appears as a white line to extract the information near the sample edge). The magnitude of A_{ave} increases monotonically with a reduction in f, approaching the steady-state temperature modulation magnitude. The signal magnitude at low f values in the top-side configuration exceeds that in the cross-section configuration, even though the results are for the same sample. This suggests that it is difficult to obtain the magnitude of the temperature modulation at the topmost surface in the cross-section configuration due to the limitation of the spatial resolution (≈20 µm) of the thermal images and slightly rounded sample corners, and that the top-side configuration is suitable for quantitative discussions about the transverse thermoelectric conversion performance. Therefore, in the following, only the results for the top-side configuration are presented.

2.3. Magneto-Thermoelectric Effects in Artificially Tilted Multilayers

Now we are in a position to discuss the contributions of the magneto-thermoelectric effects in the artificially tilted multilayers. The temperature change due to MPE (OEE) is known to exhibit an even (odd) dependence on H. Thus, to quantify the MPE and OEE contributions, we acquired LIT images under positive and negative magnetic fields and separated the H-even-dependent component from the H-odd-dependent component using the following equations:

$$A_{\mathrm{even}} = \left| A(+H)\, e^{-i\phi(+H)} + A(-H)\, e^{-i\phi(-H)} \right| /2 \tag{1}$$

$$\phi_{\mathrm{even}} = -\arg \left[A(+H)\, e^{-i\phi(+H)} + A(-H)\, e^{-i\phi(-H)} \right] \tag{2}$$

$$A_{\mathrm{odd}} = \left| A(+H)\, e^{-i\phi(+H)} - A(-H)\, e^{-i\phi(-H)} \right| /2 \tag{3}$$

$$\phi_{\mathrm{odd}} = -\arg \left[A(+H)\, e^{-i\phi(+H)} - A(-H)\, e^{-i\phi(-H)} \right] \tag{4}$$

Here, A_{even} (A_{odd}) and ϕ_{even} (ϕ_{odd}) respectively represent the lock-in amplitude and phase exhibiting the H-even (H-odd) dependence, which includes the MPE (OEE) contribution (note that the H-independent contribution is included in A_{even} and ϕ_{even}).[32,37]

Figure 3a,b shows the raw A and ϕ images for Sample A in the top-side configuration at $f = 1.0$ Hz and $\mu_0H = 0.8$ T (a, $\mathbf{H} \parallel +y$ direction) and −0.8 T (b, $\mathbf{H} \parallel -y$ direction). By substituting the data in the raw images into Equations (1)–(4), we obtained the A_{even} (A_{odd}) and ϕ_{even} (ϕ_{odd}) images at $\mu_0|H| = 0.8$ T, as shown in Figure 3c (3d). The H-even- and H-odd-dependent components exhibit different temperature distributions, suggesting that the temperature changes are caused by several different thermoelectric effects.

Figure 4c shows the $|H|$ dependence of the A_{even} signal for Sample A around the $Bi_{88}Sb_{12}/Bi_{0.2}Sb_{1.8}Te_3$ interface position, marked with a white rectangle in Figure 4a, at $f = 1.0$ Hz. With an increase in $|H|$, the A_{even} signal increases monotonically, while the ϕ_{even} values remain constant (Figure 4b,d). This non-saturating magnetic-field dependence is consistent with the behavior of the magneto-Seebeck effect, i.e., the reciprocal of MPE, in $Bi_{88}Sb_{12}$ (Figure S1a,b in the Supporting Information). Thus, we conclude that the field-induced enhancement of the A_{even} signals in the artificially tilted $Bi_{88}Sb_{12}/Bi_{0.2}Sb_{1.8}Te_3$ multilayer is due to MPE in $Bi_{88}Sb_{12}$.

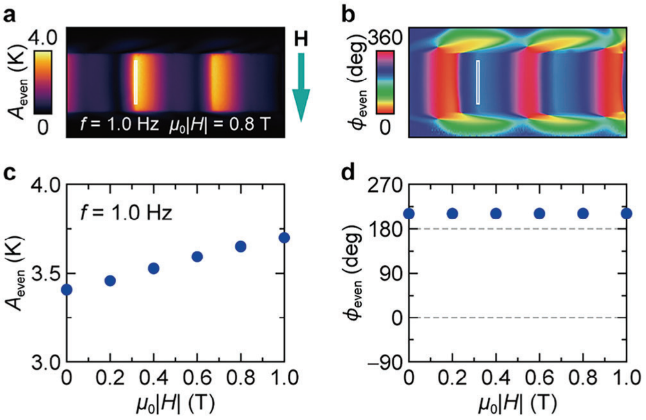

Figure 4. Contribution of MPE. a,b) A_{even} (a) and ϕ_{even} (b) images for Sample A at $f = 1.0$ Hz and $\mu_0|H| = 0.8$ T in the top-side configuration. c,d) $|H|$ dependence of the A_{even} (c) and ϕ_{even} (d) signals at $f = 1.0$ Hz. The data points in (c) and (d) were obtained by averaging the temperature modulation signals in the area defined by the white rectangles with a size of 6 × 101 pixels in (a,b), respectively.

Figure 5a,b shows the A_{odd} and ϕ_{odd} images for Sample A at $\mu_0|H| = 0.8$ T for different values of f. Clear A_{odd} signals appear only in the $\mathrm{Bi_{88}Sb_{12}}$ regions and their magnitudes increase with a reduction in f (Figure 5c). As shown in Figure 3c,d, the positions of the A_{odd} signals deviated from those of the A_{even} signals. The almost uniform ϕ_{odd} values of ≈180° at low f indicate that the transverse thermoelectric cooling also occurs in the H-odd-dependent component (see the bottom image in Figure 5b and the f dependence of ϕ_{odd} in Figure 5d). The $|H|$ dependence of the A_{odd} signal for Sample A in the $\mathrm{Bi_{88}Sb_{12}}$ region, marked with a white rectangle in Figure 5a, at $f = 1.0$ Hz is plotted as blue circles in Figure 5e. The A_{odd} signal increases with increasing $|H|$ and becomes saturated for $\mu_0|H| > 0.6$ T, while the ϕ_{odd} values remain constant (Figure 5e,f). This behavior is consistent with the magnetic-field dependence of the transverse thermopower due to the ordinary Nernst effect, i.e., the reciprocal of OEE, in $\mathrm{Bi_{88}Sb_{12}}$ (see the black curve in Figure 5e; Figure S2, Supporting Information). This result confirms that OEE also gives rise to the transverse thermoelectric conversion in the artificially tilted $\mathrm{Bi_{88}Sb_{12}/Bi_{0.2}Sb_{1.8}Te_3}$ multilayer.

Because the total output is important for actual thermoelectric applications, we next estimated the H dependence on the temperature modulation signal averaged over one $\mathrm{Bi_{88}Sb_{12}/Bi_{0.2}Sb_{1.8}Te_3}$ pair, i.e., A_{ave}, which includes structure-induced ODPE, MPE, and OEE. **Figure 6**a shows the A_{ave} signal as a function of H for Sample A at $f = 0.1$ Hz. The magnitude of A_{ave} exhibits a clear H dependence and is increased by applying a positive field owing to the superposition of MPE and OEE. As indicated by the closed circles in Figure 6b, the H-induced enhancement ratio for Sample A is estimated to be $\delta \equiv [A_{\mathrm{ave}}(H) - A_{\mathrm{ave}}(0\ \mathrm{T})]/A_{\mathrm{ave}}(0\ \mathrm{T}) \approx 11\%$ for $\mu_0 H > 0.6$ T. The δ value can be further increased by optimizing θ and t for the artificially tilted multilayers. To demonstrate this, we performed the same measurements on Sample B with different θ and t values. The open-circle data points in Figure 6b indicate that δ reaches ≈15% for Sample B at $\mu_0 H = 1.0$ T (see also the raw LIT data for Sample B in Figure S4, Supporting Information).

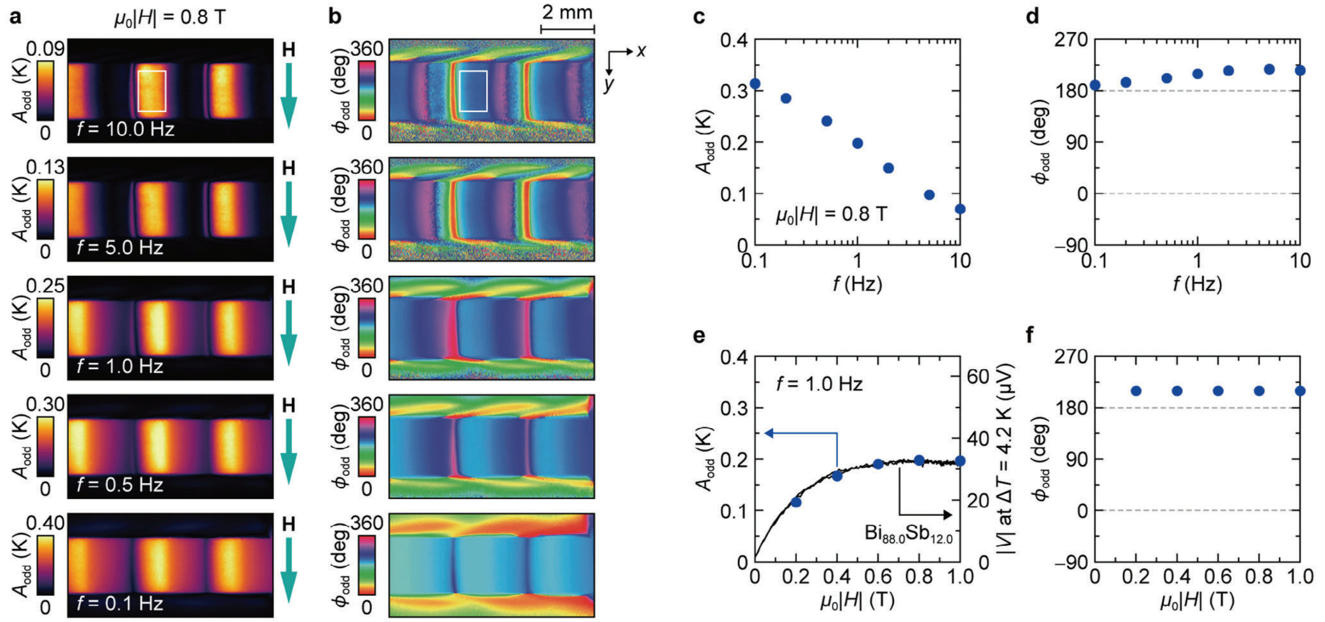

Figure 5. Contribution of OEE. a,b) A_{odd} (a) and ϕ_{odd} (b) images for Sample A at $\mu_0|H| = 0.8$ T for different values of f in the top-side configuration. c,d) f dependence of the A_{odd} (c) and ϕ_{odd} (d) signals at $\mu_0|H| = 0.8$ T. e,f) $|H|$ dependence of the A_{odd} (e) and ϕ_{odd} (f) signals at $f = 1.0$ Hz (blue circles). The black curve in (e) shows the $|H|$ dependence of the magnitude of the transverse thermoelectric voltage $|V|$ for a $\mathrm{Bi_{88}Sb_{12}}$ slab at a temperature difference of $\Delta T = 4.2$ K (see also Figure S2, Supporting Information). The data points in (c–f) were obtained by averaging the temperature modulation signals in the areas defined by the white rectangles with a size of 69 × 101 pixels in (a,b).

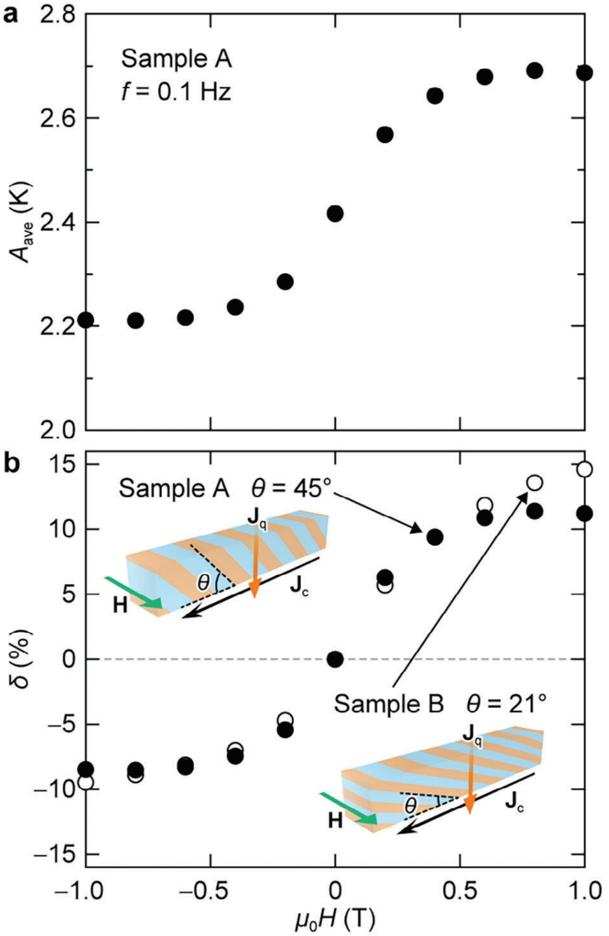

Figure 6. Magnetic-field dependence of averaged temperature modulation. a) H dependence of the A_{ave} signal for Sample A at f = 0.1 Hz. b) H dependence of $\delta \equiv [A_{ave}(H) - A_{ave}(0\ \mathrm{T})]/A_{ave}(0\ \mathrm{T})$ for Sample A (closed circles) and Sample B (open circles), i.e., the artificially tilted $Bi_{88}Sb_{12}/Bi_{0.2}Sb_{1.8}Te_3$ multilayer with θ = 21° and 0.5-mm-thick layers, at f = 0.1 Hz. The data points in this figure were obtained by averaging the temperature modulation signals in the area defined by the white rectangle in Figure 2k.

2.4. Steady-State Hybrid Transverse Magneto-Thermoelectric Cooling

The experiments presented in Section 2.3 revealed that both MPE and OEE enhance the transverse thermoelectric conversion in artificially tilted multilayers. Here, we demonstrate that the hybrid transverse magneto-thermoelectric conversion is useful for steady-state cooling. Although the contribution of Joule heating was excluded in the LIT measurements, the competition between the thermoelectric effects and Joule heating must be considered under steady-state conditions. We measured the current-induced temperature change ΔT_{ave} from room temperature averaged over the $Bi_{88}Sb_{12}/Bi_{0.2}Sb_{1.8}Te_3$ junction with a constant charge current I applied along the x direction. To obtain steady-state ΔT_{ave} values, the temperature of the sample surface was recorded after waiting 30 s from the I application using standard thermography instead of LIT. **Figure 7**a shows the ΔT_{ave} values as a function of I for Sample B at $\mu_0 H$ = 0.8 and −0.8 T. The shifted parabolic ΔT_{ave}–I curves indicate that ΔT_{ave} is determined by the competition between the thermoelectric effects (∝ I) and Joule heating (∝ I^2). The region ΔT_{ave} <0 K for I >0 A corresponds to steady-state cooling, in which the contribution of thermoelectric cooling exceeds that of Joule heating. Importantly, the ΔT_{ave}–I curves exhibit a significant shift depending on H; the steady-state cooling performance is improved by applying a positive field, where the maximum value of ΔT_{ave} = −6 K occurs at I = 5 A. The contributions of the thermoelectric effects and Joule heating can be estimated from $\Delta T_{TE} = [\Delta T(+I) - \Delta T(-I)]/2$ and $\Delta T_J = [\Delta T(+I) + \Delta T(-I)]/2$, respectively, where $\Delta T(+I)$ [$\Delta T(-I)$] denotes the ΔT_{ave} value at a positive (negative) current. As expected, the ΔT_{TE} signal is proportional to I, whereas the ΔT_J signal is proportional to I^2 (Figure 7b,c). The magnitude of ΔT_{TE} is enhanced by applying positive H owing to the contributions of the magneto-thermoelectric effects, but ΔT_J is independent of the sign of H because the magnetoresistance exhibits the H-even dependence (Figure S1c,d in the Supporting Information). As the relative

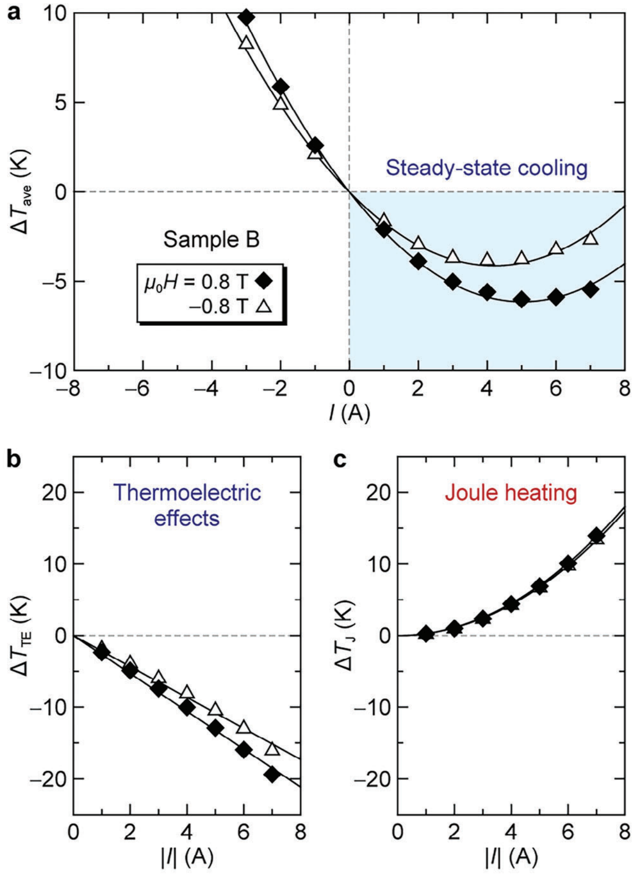

Figure 7. Steady-state hybrid transverse magneto-thermoelectric cooling. a) Charge-current I dependence of ΔT_{ave}, i.e., the steady-state temperature change from room temperature averaged over one $Bi_{88}Sb_{12}/Bi_{0.2}Sb_{1.8}Te_3$ pair, at $\mu_0 H$ = 0.8 T (diamonds) and −0.8 T (triangles). b) |I| dependence of ΔT_{TE}, i.e., the steady-state temperature change from room temperature induced by the thermoelectric effects. c) |I| dependence of ΔT_J, i.e., the steady-state temperature change from room temperature induced by Joule heating.

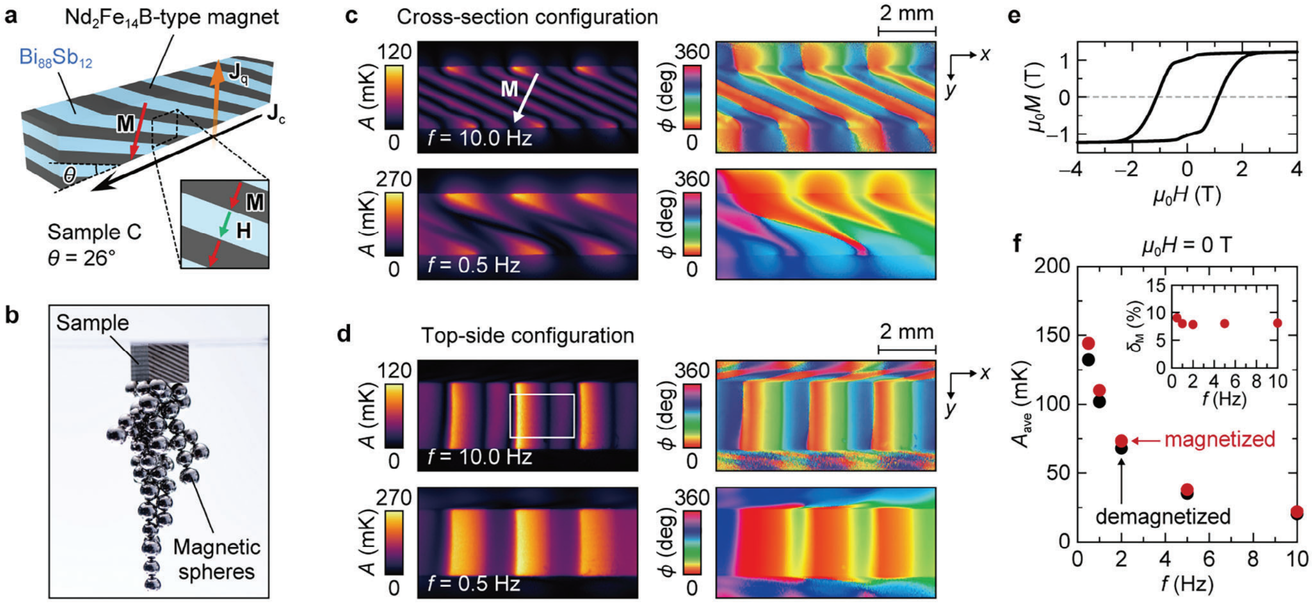

Figure 8. Transverse thermoelectric conversion in an artificially tilted multilayer based on permanent magnets. a) Schematic of Sample C, i.e., the artificially tilted $Bi_{88}Sb_{12}/Nd_2Fe_{14}B$ multilayer with $\theta = 26°$ and 0.5-mm-thick layers, in the top-side configuration. **M** denotes the spontaneous magnetization of the $Nd_2Fe_{14}B$-type magnets. b) Photograph of the artificially tilted $Bi_{88}Sb_{12}/Nd_2Fe_{14}B$ multilayer block with magnetic metal spheres attached by attraction due to the remanent magnetization of the $Nd_2Fe_{14}B$-type magnets. c,d) A and ϕ images for Sample C with the magnetized $Nd_2Fe_{14}B$-type magnet layers at $f = 10.0$ and 0.5 Hz in the cross-section (c) and top-side (d) configurations. e) H dependence of the magnetization M of the $Nd_2Fe_{14}B$-type magnet at room temperature. f) f dependence of the A_{ave} signal for Sample C with the magnetized (red circles) and demagnetized (black circles) $Nd_2Fe_{14}B$-type magnet layers in the top-side configuration. The inset of (f) shows the f dependence of $\delta_{\mathrm{M}} = (A_{\mathrm{ave,mag}} - A_{\mathrm{ave,demag}})/A_{\mathrm{ave,demag}}$, where $A_{\mathrm{ave,mag}}$ ($A_{\mathrm{ave,demag}}$) denotes A_{ave} in the magnetized (demagnetized) state. The data points in (f) were obtained by averaging the temperature modulation signals in the area defined by the white rectangle with a size of 150 × 101 pixels in (d). All the LIT data in this figure were measured in the absence of an external magnetic field.

contributions of the thermoelectric effects and Joule heating depend on the thermal boundary conditions, the steady-state cooling performance can be improved by optimizing the thermal design of the device.

2.5. Estimation of Figure of Merit

In this section, we estimate the magnetic-field dependence of the figure of merit for the artificially tilted $Bi_{88}Sb_{12}/Bi_{0.2}Sb_{1.8}Te_3$ multilayer. The figure of merit $Z_{\mathrm{T}}T$ for transverse thermoelectric conversion is defined as:

$$Z_{\mathrm{T}}T = \frac{S_{\mathrm{T}}^2 \sigma_{xx}}{\kappa_{zz}} T \tag{5}$$

where S_{T}, σ_{xx}, and κ_{zz} represent the total transverse thermopower, effective electrical conductivity along the charge current (x-direction), and effective thermal conductivity along the heat current (z-direction), respectively. The transverse thermopower due to structure-induced ODPE, σ_{xx}, and κ_{zz} can be calculated analytically using equations in the literature.[18–27] The contributions of MPE and the electrical and thermal magnetoresistances can be introduced as the field dependence of the transport coefficients in the equations for determining the ODPE-driven transverse thermopower, σ_{xx}, and κ_{zz}. However, in our artificially tilted multilayers, S_{T} includes not only the structure-induced ODPE and MPE contributions but also the OEE contribution. Analytical calculation of the OEE contribution is difficult because of the nonuniform flows of charge and heat currents. Therefore, we measured the transverse thermoelectric voltage in Samples A and B by applying a temperature gradient and magnetic field and experimentally estimated the S_{T} values (Figure S5, Supporting Information). By combining the measured S_{T} values with the calculated σ_{xx} and κ_{zz} values, we determined the figures of merit for Sample A (Sample B) at 300 K to be $Z_{\mathrm{T}}T = 0.20$, 0.17, and 0.14 (0.15, 0.13, and 0.10) at $\mu_0 H = 0.8$, 0, and −0.8 T, respectively. These results confirm that $Z_{\mathrm{T}}T$ in the artificially tilted multilayers can be enhanced by the magneto-thermoelectric effects.

2.6. Hybrid Transverse Magneto-Thermoelectric Conversion in Artificially Tilted Multilayer Based on Permanent Magnets

Despite the usefulness of the magneto-thermoelectric effects, the application of an external magnetic field often hinders thermoelectric applications. To overcome this problem, we demonstrate hybrid transverse magneto-thermoelectric conversion in the absence of an external magnetic field by incorporating permanent magnets into an artificially tilted multilayer. **Figure 8**a shows a schematic of the artificially tilted $Bi_{88}Sb_{12}/Nd_2Fe_{14}B$ multilayer with anisotropic $Nd_2Fe_{14}B$-type magnets that can be magnetized only in the direction perpendicular to the stacking plane. When the $Nd_2Fe_{14}B$ layers are magnetized, stray fields due to the remanent magnetization of the $Nd_2Fe_{14}B$ layers are applied to the $Bi_{88}Sb_{12}$ layers, which drive the magneto-thermoelectric effects in $Bi_{88}Sb_{12}$. The photograph in Figure 8b shows that the block of the artificially tilted $Bi_{88}Sb_{12}/Nd_2Fe_{14}B$ multilayer functions as a permanent magnet; the $Nd_2Fe_{14}B$ layers exhibit a strong coercive force and remanent magnetization even after bonding them with the $Bi_{88}Sb_{12}$ layers (Figure 8e). Sample C was cut from this large block.

Figure 8c (8d) shows the A and ϕ images for Sample C at $f = 10.0$ and 0.5 Hz in the cross-section (top-side) configuration. Although the temperature distributions for Sample C are qualitatively similar to those for Samples A and B, the sign of the transverse thermoelectric conversion for Sample C is opposite to that for Samples A and B because the Seebeck/Peltier coefficient of the $Nd_2Fe_{14}B$-type magnet is opposite in sign to that of $Bi_{0.2}Sb_{1.8}Te_3$ (Table 1). Figure 8f presents a comparison of the f dependence of the A_{ave} signals at $\mu_0 H = 0$ T for Sample C measured before and after magnetizing the $Nd_2Fe_{14}B$ layers. The magnitude of the temperature change is significantly increased by magnetizing the $Nd_2Fe_{14}B$ layers over the entire f range, confirming the contribution of the magneto-thermoelectric effects. As shown in the inset of Figure 8f, the magnetization-dependent enhancement ratio for Sample C is estimated to be $\delta_{\mathrm{M}} = (A_{\mathrm{ave,mag}} - A_{\mathrm{ave,demag}})/A_{\mathrm{ave,demag}} \approx 8\%$ in the absence of an external field, where $A_{\mathrm{ave,mag}}$ ($A_{\mathrm{ave,demag}}$) denotes the A_{ave} value in the magnetized (demagnetized) state. Because of the small Seebeck/Peltier coefficient of the $Nd_2Fe_{14}B$-type magnet, the magnitude of the A_{ave} signals for Sample C is one order of magnitude smaller than that for Samples A and B. Nevertheless, this experiment clearly indicates that the hybrid transverse magneto-thermoelectric conversion can be achieved without an external magnetic field, suggesting the importance of developing permanent magnets with large Seebeck/Peltier coefficients to realize efficient transverse thermoelectric conversion. The transverse thermoelectric conversion performance in the artificially tilted multilayers based on permanent magnets may also be improved by stacking three different materials, i.e., a permanent magnet and p- and n-type conductors showing large Seebeck/Peltier coefficients as well as large magneto-thermoelectric effects.

Finally, we discuss the origin of the magnetization-dependent enhancement of the transverse thermoelectric conversion in the artificially tilted multilayer based on permanent magnets. Although the remanent magnetization of the $Nd_2Fe_{14}B$ layers generates a magnetic field in the $Bi_{88}Sb_{12}$ layers, the configuration in Figure 8a does not satisfy the symmetry of OEE because of the absence of the magnetization component in the direction of the cross product of $\mathbf{J}_{\mathrm{c}}$ and $\mathbf{J}_{\mathrm{q}}$. Thus, in Sample C, MPE is expected to manifest directly. However, because the stray field is non-uniform near the surfaces of the sample, a finite OEE contribution may also appear. To optimize artificially tilted multilayers based on permanent magnets, the design of not only transverse thermoelectric properties but also stray-field distributions is required. The use of isotropic magnets facilitates the control of the stray-field distributions.

3. Conclusion

We demonstrated the hybrid transverse thermoelectric cooling by multiple phenomena including the magneto-thermoelectric effects in artificially tilted multilayers. Using the thermoelectric imaging technique based on LIT, the transverse thermoelectric cooling processes in the artificially tilted $Bi_{88}Sb_{12}/Bi_{0.2}Sb_{1.8}Te_3$ multilayers were clarified. The LIT measurements under magnetic fields allowed us to separate the contributions of the magneto-thermoelectric effects exhibiting the even dependence on the magnetic field, i.e., MPE, and odd dependence, i.e., OEE, from the field-independent ODPE contribution. Through the systematic measurements and analyses, we quantified the contributions of each magneto-thermoelectric effect, and found that both MPE and OEE can improve the steady-state cooling capability and figure of merit of the artificially tilted multilayers. Furthermore, by replacing one of the constituent materials in the multilayer with permanent magnets, we demonstrated that hybrid transverse magneto-thermoelectric conversion can operate even in the absence of a magnetic field. The artificially tilted multilayers based on permanent magnets function as "thermoelectric permanent magnets" that have high transverse thermoelectric conversion performance together with spontaneous magnetization. This concept provides an unconventional strategy for increasing the transverse magneto-thermoelectric conversion efficiency and suggests the possibility of transforming omnipresent permanent magnets into functional materials that enable electronic cooling and thermopower generation. Practical applications of the hybrid transverse magneto-thermoelectric conversion require the development of stable n- and p-type materials that exhibit large magneto-thermoelectric effects, simultaneous achievement of the large magneto-thermoelectric conversion and its zero-field operation, reduction of the thermal conductivity by nanostructuring or phonon engineering,[38,39] and development of module structures suitable for this operation principle.

4. Experimental Section

Sample Preparation and Characterization: Samples A and B, i.e., the artificially tilted $Bi_{88}Sb_{12}/Bi_{0.2}Sb_{1.8}Te_3$ multilayers, were prepared as follows. First, homogenous $Bi_{88}Sb_{12}$ and $Bi_{0.2}Sb_{1.8}Te_3$ alloy slabs were synthesized. BiSb alloy powder (99.99% purity), obtained from Kojundo Chemical Laboratory Co., Ltd., was crushed using a planetary ball mill (PL-7, Fritsch Japan Co., Ltd.) at 350 rpm for 30 min. The crushed powder was then sieved through a 63-µm mesh. Next, a cylindrical $Bi_{88}Sb_{12}$ ingot with a diameter of 10 mm was prepared via the SPS method under a pressure of 50 MPa at 245 °C for 5 min in vacuum conditions. A cylindrical $Bi_{0.2}Sb_{1.8}Te_3$ ingot with a diameter of 10 mm was also prepared via the SPS method under a pressure of 30 MPa at 445 °C for 4 min in vacuum conditions by using BiSbTe alloy powder (99.9% purity) with a particle size of <74 µm, which was obtained from Toshima Manufacturing Co., Ltd. The $Bi_{88}Sb_{12}$ and $Bi_{0.2}Sb_{1.8}Te_3$ alloys are polycrystalline and their grain crystal orientations are random, indicating isotropic transport properties. Using a diamond wire saw, the ingots were sliced into many disks with a thickness of 1 mm (0.5 mm) for Sample A (Sample B). The $Bi_{88}Sb_{12}$ and $Bi_{0.2}Sb_{1.8}Te_3$ discs were alternately stacked and bonded via the SPS method under a pressure of 30 MPa at 230 °C for 5 h. Finally, the bonded stack was cut into a rectangular shape with a size of $\approx 10 \times 2 \times 2$ mm^3 and $\theta = 45°$ ($\theta = 21°$) for Sample A (Sample B) using the diamond wire saw. The elemental distributions and compositions of Samples A and B were characterized by scanning electron microscopy (SEM) and energy-dispersive X-ray spectroscopy (EDS) using Cross-Beam 1540ESB (Carl Zeiss AG). The samples for the SEM observations were prepared via mechanical polishing. As shown in Figure S6 (Supporting Information), the compositions of the bulk regions of $Bi_{88}Sb_{12}$ and $Bi_{0.2}Sb_{1.8}Te_3$

were uniform, although an interdiffusion of ≈30 µm in width was observed at the interfaces. Considering the large sample size, it is concluded that the artificially tilted $Bi_{88}Sb_{12}/Bi_{0.2}Sb_{1.8}Te_3$ multilayers have sharp boundaries.

Sample C, i.e., the artificially tilted $Bi_{88}Sb_{12}/Nd_2Fe_{14}B$ multilayer, was prepared as follows. $Bi_{88}Sb_{12}$ discs with a diameter of 20 mm and thickness of 0.5 mm were prepared by the same method used for Samples A and B. Ni/Cu/Ni-plated anisotropic $Nd_2Fe_{14}B$-type magnet discs were employed with a diameter of 20 mm and thickness of 0.5 mm, which were obtained from Magfine Corporation. The $Bi_{88}Sb_{12}$ and $Nd_2Fe_{14}B$-type magnet discs were alternately stacked and bonded via the SPS method under a pressure of 20 MPa at 245 °C for 1 h. The $Nd_2Fe_{14}B$-type magnets were demagnetized before the bonding process. The bonded stack was cut into a rectangular shape with a size of $\approx 10 \times 2 \times 2$ mm^3 and $\theta = 26°$ using the diamond wire saw. The elemental distribution in Sample C was characterized by SEM-EDS. Owing to the presence of the plating layers, the interdiffusion between the $Bi_{88}Sb_{12}$ and $Nd_2Fe_{14}B$-type magnets was negligible (Figure S7, Supporting Information). As boron could not be detected by SEM-EDS, the composition of the $Nd_2Fe_{14}B$-type magnets without plating layers was measured by means of inductively coupled plasma analysis. The composition was determined to be $Nd_{8.3}Pr_{2.7}Ce_{3.4}Gd_{0.7}Fe_{77.2}Co_{0.3}B_{5.9}Cu_{0.2}Al_{1.3}$ (at%), where the oxygen concentration was not analyzed. The anisotropic $Nd_2Fe_{14}B$-type magnets can only be magnetized in their magnetic easy axis, i.e., the direction perpendicular to the stacking plane. To verify that the magnetic properties of the $Nd_2Fe_{14}B$ layers were not degraded after sinter-bonding, the $Nd_2Fe_{14}B$-type magnet portion was cut from the multilayer, and its magnetization curve was measured by superconducting quantum interference device vibrating sample magnetometry using Magnetic Properties Measurement System (MPMS3, Quantum Design Inc.).

Thermography Measurements: The LIT measurements were performed using Enhanced Lock-In Thermal Emission (ELITE, DCG Systems G.K.) at room temperature and atmospheric pressure. For the LIT measurements, the sample was fixed on a plastic plate with low thermal conductivity to reduce the heat leakage due to thermal conduction. To enhance the infrared emissivity and ensure uniform emission properties, the top surface of the sample was coated with insulating black ink having an emissivity of >0.94 (JSC-3, JAPANSENSOR Corporation). As described above, Sample C was synthesized after demagnetizing the $Nd_2Fe_{14}B$ layers. Therefore, the LIT data were first obtained in the demagnetized state. Then, the $Nd_2Fe_{14}B$ layers were magnetized in the direction perpendicular to the stacking plane by a pulsed magnetic field of 8 T, and the LIT measurements were performed for the same sample under the same conditions. During the systematic LIT measurements, all the samples were stable; the thermoelectric response did not change by repeating heating-cooling cycles.

The steady-state thermography measurements were performed for obtaining the data in Figure 7 using a different infrared camera (ImageIR 8300, InfraTec GmbH). To reduce the Joule heating contribution, Sample B was fixed on an Al block whose surface was anodized because Al has a high thermal conductivity. Similar to the LIT measurements, the top surface of the sample was coated with black ink.

Measurements of Transport Properties: The longitudinal electric conductivity of the materials used in this study was measured by the four-probe method. The thermal conductivity was determined through thermal diffusivity measured by the laser flash method, specific heat measured by the differential scanning calorimetry, and density measured by the Archimedes method. The Seebeck coefficient and its magnetic-field dependence were measured using the method described in ref. [40]. Here, the sample was clamped between two Cu blocks of which the temperatures were controlled independently with ceramic heaters and temperature sensors. For accurate measurements of the Seebeck coefficient, an applied temperature difference and generated thermoelectric voltage at the same positions were measured simultaneously by using two pairs of thermocouple probes attached to the sample, where the temperature difference (thermoelectric voltage) was estimated from voltage outputs in each thermocouple (between the probes). This system is similar to the Seebeck Coefficient/Electric Resistance Measurement System (ZEM-3, ADVANCE RIKO, Inc.) but in the system, a magnetic field can be applied in the direction perpendicular to the temperature gradient.[40] After stabilizing the temperatures of the Cu blocks, the Seebeck coefficient of the sample was estimated by fitting the temperature difference dependence of the thermoelectric voltage with a linear function at room temperature at various values of H. The obtained Seebeck coefficient and figure of merit for the Seebeck effect of $Bi_{88}Sb_{12}$ and $Bi_{0.2}Sb_{1.8}Te_3$ are consistent with the values in the literature[36,37,41] (note that techniques to increase the figure of merit, e.g., reduction of the thermal conductivity by nanostructuring or phonon engineering[38,39] and enhancement of the Seebeck coefficient by energy filtering through nano-compositing, are not applied to the materials used in this study). The ordinary Nernst effect of $Bi_{88}Sb_{12}$ and $Bi_{0.2}Sb_{1.8}Te_3$ was measured using a homemade temperature gradient generator combined with an electromagnet via a method similar to that described in ref. [17]. A rectangular sample was bridged and fixed on two anodized Al blocks. One of the Al blocks is thermally connected to a heat bath and the other to a chip heater, where a temperature gradient can be generated by applying a charge current to the heater. The surface of the sample was coated with black ink and the magnitude of the applied temperature gradient was measured with the infrared camera. While the magnetic field was swept in the direction perpendicular to the temperature gradient, the electric voltage in the direction perpendicular to both the temperature gradient and **H** was measured. The anomalous Nernst coefficient of the $Nd_2Fe_{14}B$-type magnet, shown in Table 1, was estimated through the LIT measurements of the anomalous Ettingshausen effect and the Onsager reciprocal relation.[10] These measurements were performed at room temperature and atmospheric pressure using the materials prepared under the same conditions as those used for Samples A, B, and C.

Supporting Information

Supporting Information is available from the Wiley Online Library or from the author.

Acknowledgements

The authors thank Y. Oikawa for valuable discussions, and K. Suzuki, M. Isomura, and X. Tang for technical support. This work was supported by ERATO "Magnetic Thermal Management Materials" (grant no. JPMJER2201) from JST, Japan.

Conflict of Interest

The authors declare no conflict of interest.

Author Contributions

K.U. planned and supervised the study, designed the experiments, prepared the samples, performed the LIT measurements, developed the explanation of the experiments, and prepared the manuscript. K.U., T.H., and F.A. collected the thermal, thermoelectric, and magnetic properties of the samples. T.H. analyzed the LIT data. F.A. analytically calculated the transverse thermoelectric conversion properties. H.S.A. performed the microstructure analyses. All the authors discussed the results and commented on the manuscript.

Data Availability Statement

The data that support the findings of this study are available from the corresponding author upon reasonable request.

Keywords

artificially tilted multilayers, Ettingshausen effect, lock-in thermography, magneto-Peltier effect, permanent magnets, transverse thermoelectrics

Received: July 24, 2023
Revised: October 9, 2023
Published online: November 29, 2023

[1] D. Zhao, G. Tan, *Appl. Therm. Eng.* **2014**, *66*, 15.
[2] Q. Yan, M. G. Kanatzidis, *Nat. Mater.* **2022**, *21*, 503.
[3] K. Uchida, J. P. Heremans, *Joule* **2022**, *6*, 2240.
[4] A. V. Ettingshausen, W. Nernst, *Ann. Phys.* **1886**, *265*, 343.
[5] K. F. Cuff, R. B. Horst, J. L. Weaver, S. R. Hawkins, C. F. Kooi, G. M. Enslow, *Appl. Phys. Lett.* **1963**, *2*, 145.
[6] T. C. Harman, J. M. Honig, S. Fischler, A. E. Paladino, M. J. Button, *Appl. Phys. Lett.* **1964**, *4*, 77.
[7] P. Jandl, U. Birkholz, *J. Appl. Phys.* **1994**, *76*, 7351.
[8] Y. Sakuraba, *Scr. Mater.* **2016**, *111*, 29.
[9] A. Sakai, Y. P. Mizuta, A. A. Nugroho, R. Sihombing, T. Koretsune, M.-T. Suzuki, N. Takemori, R. Ishii, D. Nishio-Hamane, R. Arita, P. Goswami, S. Nakatsuji, *Nat. Phys.* **2018**, *14*, 1119.
[10] A. Miura, H. Sepehri-Amin, K. Masuda, H. Tsuchiura, Y. Miura, R. Iguchi, Y. Sakuraba, J. Shiomi, K. Hono, K. Uchida, *Appl. Phys. Lett.* **2019**, *115*, 222403.
[11] K. Uchida, W. Zhou, Y. Sakuraba, *Appl. Phys. Lett.* **2021**, *118*, 140504.
[12] Y. Pan, C. Le, B. He, S. J. Watzman, M. Yao, J. Gooth, J. P. Heremans, Y. Sun, C. Felser, *Nat. Mater.* **2022**, *21*, 203.
[13] M. R. Scudder, B. He, Y. Wang, A. Rai, D. G. Cahill, W. Windl, J. P. Heremans, J. E. Goldberger, *Energy Environ. Sci.* **2021**, *14*, 4009.
[14] K. Uchida, S. Takahashi, K. Harii, J. Ieda, W. Koshibae, K. Ando, S. Maekawa, E. Saitoh, *Nature* **2008**, *455*, 778.
[15] J. Flipse, F. K. Dejene, D. Wagenaar, G. E. W. Bauer, J. B. Youssef, B. J. Van Wees, *Phys. Rev. Lett.* **2014**, *113*, 027601.
[16] S. Daimon, R. Iguchi, T. Hioki, E. Saitoh, K. Uchida, *Nat. Commun.* **2016**, *7*, 13754.
[17] W. Zhou, K. Yamamoto, A. Miura, R. Iguchi, Y. Miura, K. Uchida, Y. Sakuraba, *Nat. Mater.* **2021**, *20*, 463.
[18] T. h. Zahner, R. Förg, H. Lengfellner, *Appl. Phys. Lett.* **1998**, *73*, 1364.
[19] D. M. Rowe, *Thermoelectrics Handbook Macro to Nano*, CRC Press, New York, USA **2006**.
[20] T. Kanno, S. Yotsuhashi, A. Sakai, K. Takahashi, H. Adachi, *Appl. Phys. Lett.* **2009**, *94*, 061917.
[21] H. J. Goldsmid, *J. Electron. Mater.* **2011**, *40*, 1254.
[22] T. Kanno, A. Sakai, K. Takahashi, A. Omote, H. Adachi, Y. Yamada, *Appl. Phys. Lett.* **2012**, *101*, 011906.
[23] A. Sakai, T. Kanno, K. Takahashi, H. Tamaki, H. Kusada, Y. Yamada, H. Abe, *Sci. Rep.* **2014**, *4*, 6089.
[24] X. Mu, H. Zhou, W. Zhao, D. He, W. Zhu, X. Nie, Z. Sun, Q. Zhang, *J. Power Sources* **2019**, *430*, 193.
[25] Y. Li, P. Wei, H. Zhou, X. Mu, W. Zhu, X. Nie, X. Sang, W. Zhao, *J. Electron. Mater.* **2020**, *49*, 5980.
[26] H. Zhou, H. Liu, G. Qian, H. Yu, X. Gong, X. Li, J. Zheng, *Micromachines* **2022**, *13*, 233.
[27] K. Yue, W. Zhu, Q. He, X. Nie, X. Qi, C. Sun, W. Zhao, Q. Zhang, *ACS Appl. Mater. Interfaces* **2022**, *14*, 39053.
[28] G. E. W. Bauer, E. Saitoh, B. J. Van Wees, *Nat. Mater.* **2012**, *11*, 391.
[29] S. R. Boona, R. C. Myers, J. P. Heremans, *Energy Environ. Sci.* **2014**, *7*, 885.
[30] K. Uchida, *Proc. Jpn. Acad., Ser. B* **2021**, *97*, 69.
[31] O. Breitenstein, W. Warta, M. Langenkamp, *Lock-in Thermography: Basics and Use for Evaluating Electronic Devices and Materials Introduction*, Springer, Berlin/Heidelberg, Germany **2010**.
[32] K. Uchida, S. Daimon, R. Iguchi, E. Saitoh, *Nature* **2018**, *558*, 95.
[33] J. P. Jan, in *Solid State Physics* (Eds: F. Seitz, D. Turnbull), Academic, New York, USA, **1957**.
[34] C. Zhou, S. Birner, Y. Tang, K. Heinselman, M. Grayson, *Phys. Rev. Lett.* **2013**, *110*, 227701.
[35] Y. Tang, B. Cui, C. Zhou, M. Grayson, *J. Electron. Mater.* **2015**, *44*, 2095.
[36] M. Murata, A. Yamamoto, Y. Hasegawa, T. Komine, *J. Electron. Mater.* **2016**, *45*, 1875.
[37] K. Uchida, M. Murata, A. Miura, R. Iguchi, *Phys. Rev. Lett.* **2020**, *125*, 106601.
[38] S. I. Kim, K. H. Lee, H. A. Mun, H. S. Kim, S. W. Hwang, J. W. Roh, D. J. Yang, W. H. Shin, X. S. Li, Y. H. Lee, G. J. Snyder, S. W. Kim, *Science* **2015**, *348*, 109.
[39] M. Nomura, J. Shiomi, T. Shiga, R. Anufriev, *Jpn. J. Appl. Phys.* **2018**, *57*, 080101.
[40] T. Hirai, R. Modak, A. Miura, T. Seki, K. Takanashi, K. Uchida, *Appl. Phys. Express* **2021**, *14*, 073001.
[41] B. Poudel, Q. Hao, Y. Ma, Y. Lan, A. Minnich, B. Yu, X. Yan, D. Wang, A. Muto, D. Vashaee, X. Chen, J. Liu, M. S. Dresselhaus, G. Chen, Z. Ren, *Science* **2008**, *320*, 634.